

An adsorbed gas estimation model for shale gas reservoirs via statistical learning

Yuntian Chen,^{a,1} Su Jiang,^{b,1} Dongxiao Zhang,^{a,*} and Chaoyang Liu^c

^a ERE and BIC-ESAT, College of Engineering, Peking University, No. 5, Yiheyuan Road, Beijing 1000871, China

^b Department of Energy Resources Engineering, Stanford University, Stanford, California 95305, U.S.A.

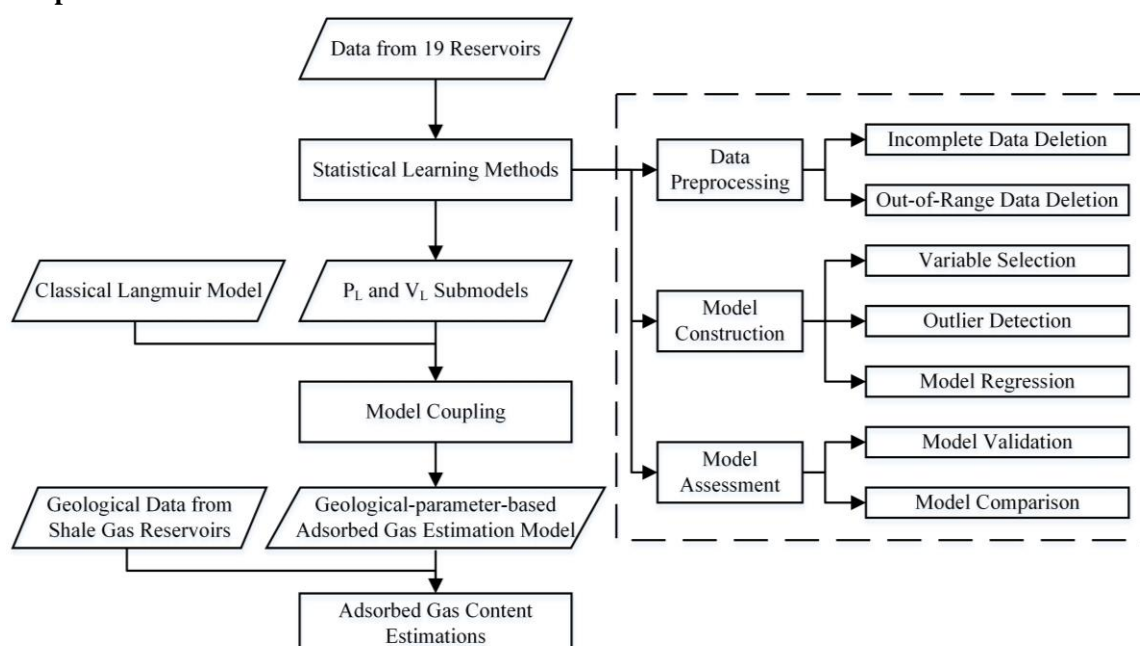
^c Department of Materials Science and Engineering, Massachusetts Institute of Technology, Cambridge, Massachusetts 02139, U.S.A.

* Corresponding author at: College of Engineering, Peking University, No. 5, Yiheyuan Road, Beijing 1000871, China. Tel.: +86 10 6275-7432; fax: +86 10 6275-6607.

E-mail address: dxz@pku.edu.cn (D. Zhang)

¹ Authors have made equal contributions to this work.

Graphical Abstract:



Keywords: shale gas; statistical learning; big data; adsorbed gas; estimation model; geological parameter.

Abstract:

Shale gas plays an important role in reducing pollution and adjusting the structure of world energy. Gas content estimation is particularly significant in shale gas resource evaluation. There exist various estimation methods, such as first principle methods and empirical models. However, resource evaluation presents many challenges, especially the insufficient accuracy of existing models and the high cost resulting from time-consuming adsorption experiments. In this research, a low-cost and high-accuracy model based on geological parameters is constructed through statistical learning methods to estimate adsorbed shale gas content. The new model consists of two components, which are used to estimate Langmuir pressure (P_L) and Langmuir volume (V_L) based on their quantitative relationships with geological parameters. To increase the accuracy of the model, a “big data” set that consists of 301 data entries was compiled and utilized. Data outliers

were detected by the K-Nearest Neighbor (K-NN) algorithm, and the model performance was evaluated by the leave-one-out algorithm. The proposed model was compared with four existing models. The results show that the novel model has better estimation accuracy than the previous ones. Furthermore, because all variables in the new model are not dependent on any time-consuming experimental methods, the new model has low cost and is highly efficient for approximate overall estimation of shale gas reservoirs. Finally, the proposed model was employed to estimate adsorbed gas content for nine shale gas reservoirs in China, Germany, and the U.S.A.

1. Introduction

Shale gas, or natural gas trapped within shale formations, is a type of relatively clean energy resource. It consists mainly of methane and burns cleaner than other kinds of hydrocarbon fuel. As an alternative fuel, shale gas is attracting increased attention globally [1-8]. Shale gas consists of free gas, adsorbed gas, and solution gas: free gas is the shale gas in the pore space within the shale rock; adsorbed gas is a significant quantity of gas adsorbed on the surface of organics and clays in the shale formation; and solution gas is the gas dissolved in the reservoir water or oil. The volume of solution gas is governed by pressure and temperature. As the pressure drops below the bubble point, the gas dissolved in the liquid begins to be released and becomes free gas. **Fig. 1** illustrates these three kinds of shale gas. In recent years, the production of shale gas has increased significantly. For instance, in 2000, shale gas only occupied 1.6% of gas production in the U.S.A. [9], while this percentage rose to 47% in 2015 [10]. In China, the total production of shale gas was only 200 million m³ in 2013. However, it increased to 1.3 billion m³ in 2014 [11] and 4.47 billion m³ in 2015 [12]. Shale gas is thus expected to play an even more critical role in the world's energy supply in the near future.

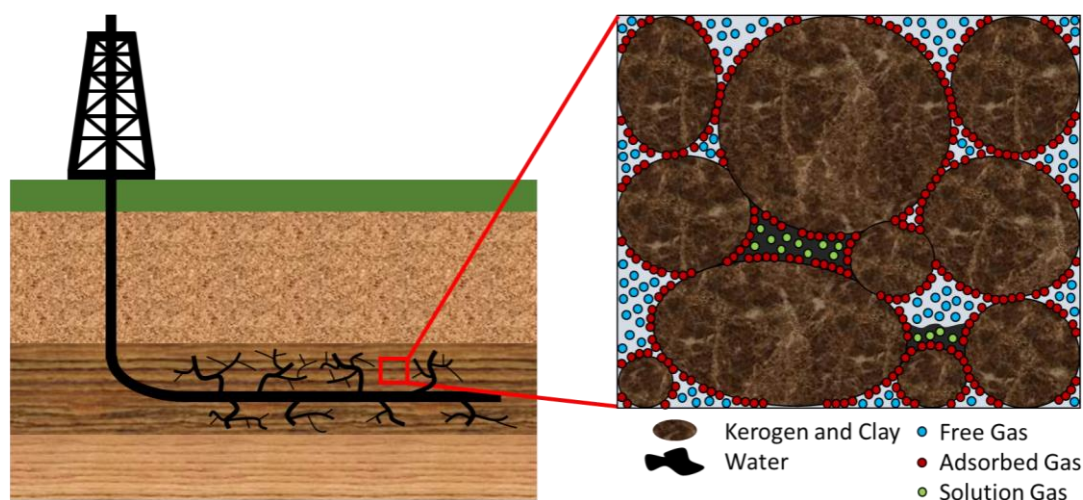


Fig. 1. Illustration of free gas, adsorbed gas, and solution gas in shale formations.

There are many challenges involved in shale gas development and evaluation processes. One of the most important problems is to provide an accurate resource estimation. For instance, the U.S. Energy Information Administration (EIA) and the Chinese Ministry of Land and Resources have quite different evaluations of China shale gas resources, which are 31.6 trillion m³ and 25.1 trillion m³, respectively [13, 14]. The uncertainty regarding resource estimation will not only

affect the gas well site selection on a micro level, but will also influence the national and industrial policy-making process on a macro level. Thus, it is crucial to find a way to accurately evaluate shale gas resources around the world. This research emphasizes adsorbed gas because it accounts for 20% to 80% of the total gas [15-17]. Adsorbed gas also includes solution gas, which is only a small portion of the total gas content [14, 18]. Regarding free gas, many researchers have already proposed accurate estimation models [18-20].

In gas content estimation, first principle methods and empirical models are common options. The first principle methods are still not thoroughly developed, because of the complexity of storage mechanisms and the lack of understanding of the influence of numerous factors, such as thermal maturity (R_o) and reservoir temperature (T). Thus, it is challenging to build an accurate theoretical model. Regarding the empirical models, the Langmuir model (**Eq. (1)**) is the most commonly used [21, 22]. Its primary advantage is that, once Langmuir pressure (P_L) and Langmuir volume (V_L) are determined, the Langmuir adsorption isothermal curve is ascertained, which makes it easy to calculate adsorbed gas content under any reservoir pressure. Nevertheless, adsorption experiments are probably the only effective methods to obtain Langmuir parameters. However, these experiments are very time-consuming, as the adsorption process within the microscale and nanoscale shale pores is slow [23], and the coring process to obtain the experiment sample is expensive. These challenges cause difficulties in determining the corresponding Langmuir parameters and high uncertainties regarding adsorbed gas content evaluation. In addition, most of these experiments are complicated and are subject to experimental errors. For example, leakage always occurs in the coring process, which affects the accuracy of the adsorption experiments. Because both the first principle methods and empirical models have difficulties in gas content estimation, the salient question is: are there any alternatives that are reasonably accurate, but do not rely on any site-specific adsorption experiments?

$$V = \frac{P \cdot V_L}{P + P_L} \quad (1)$$

In this work, we proposed to use widely available geological parameters to estimate resource volume via statistical learning. After years of development, statistical learning has become a powerful tool to build models [24-36], but it has never been applied to shale gas resource evaluation. Statistical learning is a commonly used method for Big Data Analytics, and it is effective in finding a predictive function based on a big data set. Statistical learning has many successful applications in various fields, such as computer vision, sales forecasting, and bioinformatics. It is not only utilized to uncover hidden patterns and unknown correlations between variables, but is also utilized to alleviate the influence of data uncertainty resulting from the operation process. For the problem that we are considering, geological parameters, such as total organic carbon (TOC), thermal maturity (R_o , vitrinite reflectance) and reservoir temperature (T), are much easier to obtain compared with Langmuir parameters. Thus, one promising strategy is to use these easily-obtained geological parameters to estimate the Langmuir parameters with statistical learning methods.

Attempts have been made to discern the qualitative correlation between geological parameters and Langmuir parameters. The positive correlation between V_L and TOC has been shown in the

literature [37-40], and a similar positive correlation between R_o and V_L is found [23]. The qualitative influences of TOC, R_o , and T on Langmuir parameters are revealed by Zhao et al. [41]. Regarding P_L , Kong et al. identified the effect of T, R_o and porosity on the shale gas adsorption process, and discussed the determining physical mechanisms [42]. Hao et al. studied the influence of T on P_L , as well [43]. Although the qualitative effect of different factors has been widely studied, the quantitative relationships remain unclear. Attempts have been made to use linear regression to estimate V_L with TOC as the only independent variable [44-46]. Although TOC is essential in adsorption, previous studies have shown that TOC is not the only influencing factor [23, 41]. The dataset of these works are not abundant as well. For example, there are only 7-10 data points from shale gas reservoirs in these studies. As for P_L , Xia et al. attempted to build a first principle model based on isosteric heat, standard entropy, and temperature [47]. Nevertheless, the variables used in this theoretical model are difficult to measure, which restricts model applicability. Later, Zhang et al. utilized T as an independent variable to estimate P_L [46]. T is a significant factor since adsorption is an exothermic process. However, it is not comprehensive to consider T as the only independent variable. In addition, this model's dataset only has six data points.

In conclusion, many studies in the last decade estimated Langmuir parameters by using geological parameters, but these quantitative models usually present three unresolved problems. The first one is inadequate sample size. Owing to the high cost of adsorption experiments, the datasets of previous studies are often too small to obtain a reliable and stable model. Some of these data are from coal bed methane and are not suitable for shale gas analysis [44, 46]. The second one concerns factor selection. Numerous previous studies consider factors non-comprehensively [44-46]. Specifically, most of these studies only focused on TOC. This is partially reasonable since TOC constitutes the main hydrocarbon-generation matter and gas carrier [48], but TOC alone cannot describe Langmuir parameters sufficiently, and other factors should be considered [23]. The last problem is the lack of general applicability. Most of the previous work only has data that cover a certain reservoir or even a single well, and the validation test is always overlooked [44-47]. In fact, among all of the three problems, inadequate sample size presents the biggest obstacle, as it partially causes the other two problems.

The main objective of this study is to solve the three problems above and build an adsorbed gas content estimation model based on geological parameters via statistical learning. The model-building process is shown in **Fig. 2**. To solve the inadequate sample size problem, 301 adsorption experiment data sets were compiled and analyzed from 19 different reservoirs in seven countries. Our data are much bigger than those in previous studies, which usually have less than 10 data sets. Once the sample size is enlarged, statistical learning may become more effective in the model-building process. The variables are determined by correlation analysis to solve the factor selection problem. Data outliers may be detected by the K-NN algorithm to broaden applicability [25-27, 35, 36]. In addition, model quality is assessed by the leave-one-out algorithm [28-33]. Based on the big training dataset and the statistical learning methods, this paper proposed an efficient model that does not rely on time-consuming experiments. Finally, the adsorbed gas contents from nine reservoirs in China, Germany, and the U.S.A. were estimated as case studies.

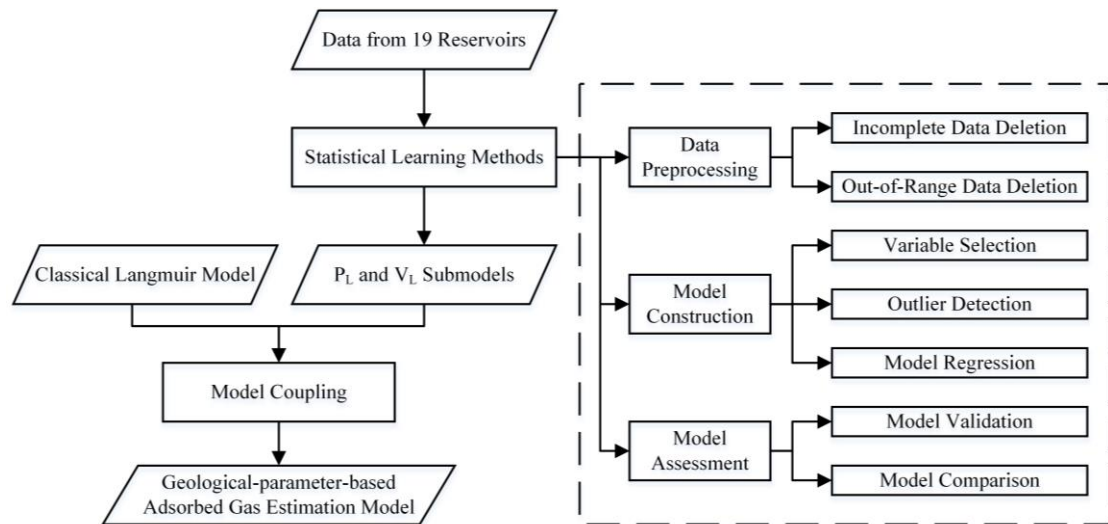


Fig. 2. Flow chart of the model-building process. The geological-parameter-based adsorbed gas estimation model is constructed by the coupling of classical Langmuir model, P_L submodel, and V_L submodel. The P_L and V_L submodels are built via statistical learning methods, which are explained in the dashed box.

2. Data description and preprocessing

The expansion of data size is necessary for developing an accurate estimation model, since it constitutes the foundation of the statistical learning process. Most existing models have no more than 10 data entries, which is not sufficient to construct a credible model. To overcome the data size restriction, raw data points are collected from 24 different studies, experiment reports, and databases in this study [23, 37, 39, 40, 44-46, 48-64]. These data are available in the online supplementary material of this paper. They are gathered from marine and terrestrial shales from various reservoirs around the world. **Table 1** shows the seven countries and 19 reservoirs used in this research. The variety of data sources makes the model suitable for general use.

Table 1
Data source information (detailed data are shown in the online supplement)

Country	Reservoirs	Literature	Amount of data points
U.S.A.	Barnett Shale	[39, 48, 57]	32
	Haynesville Shale	[39]	2
	Marcellus Shale	[57-59]	15
	Utica Shale	[59]	6
	Woodford Shale	[46]	3
	Eagle Ford Shale	[39, 57]	2
Canada	Montney Shale	[57]	2
	Besa River Formation	[59]	7
	Colorado Group Formation	[59, 63]	13
	Exshaw Formation	[59, 64]	3
	Muskwa Formation	[59, 62]	3
	Duvernay Formation	[62]	4

China	Sichuan Basin	[23, 45, 48, 49, 51-53, 55, 56]	136
	Yangtze Platform	[40]	21
	Ordos Basin	[50, 61]	18
Germany	Posidonia Shale	[39, 60]	31
Sweden	Alum Shale	[39]	20
Netherlands	Carboniferous Shale	[39]	9
Brazil	Paraná Basin	[44]	2

The raw data should be cleaned prior to use for model building. The cleaning process is explained in the online supplementary material. In this work, data preprocessing includes two straightforward steps. The first step is data cleaning, with the criterion that each data point should have both dependent variables and independent variables. According to this criterion, the P_L data point should have R_o , TOC and T data, while the V_L data point should have TOC and T data (Section 3.1 will introduce the independent variable selection method). In this step, incomplete data are deleted, and replicate data are integrated. The second step concerns the value range of geological parameters. It is reasonable to omit the out-of-range data. Previous work indicates that the TOC is always greater than 2% in promising shale gas reservoirs [13, 65]. To be conservative, 1% was taken as the floor level of TOC in this work. The R_o of promising reservoirs should be lower than 4%, otherwise it is over-matured [66-68]. Moreover, the experimental data set exhibits the following properties: i) there is little data in which TOC is greater than 17% or T is greater than 90°C; ii) P_L is usually greater than 1.5 MPa and less than 12 MPa; and iii) V_L is the maximum adsorbed gas volume, and it has to be greater than 1 m³/t for the sake of economic exploitation. Thus, the effective data point for P_L should have a temperature below 90°C, R_o less than 4%, TOC between 1% and 17%, and P_L higher than 1.5 MPa and less than 12 MPa. After data processing, there are 101 data points remaining, as shown in the supplementary material online. Regarding V_L , the effective data points should have a temperature below 90°C, TOC between 1% and 17%, and V_L higher than 1 m³/t. The data points outside of this range have to be deleted. There are then 200 data points remaining, as shown in the supplementary material online. Finally, this research's database consists of 301 data points (101 P_L data and 200 V_L data), which is much larger than previous works' databases with fewer than 10 data points [44-47].

3. Model Construction

Regression models are built to identify the quantitative relationships between Langmuir and geological parameters. The model-building method consists of the following three parts: variable selection, outlier detection, and model regression.

3.1 Variable selection

In the Langmuir equation, P_L and V_L indicate the adsorption capacity of the shale formation. V_L denotes the maximum adsorbed gas volume, and P_L represents the pressure when the adsorbed gas volume is equal to half of V_L [21]. In this work, the Langmuir parameters could be estimated by geological parameters due to the strong relationships between them. The geological variables are selected according to the data availability and their influences on P_L and V_L . Recent studies

have shown that the main influencing factors of P_L are reservoir temperature (T), total organic carbon (TOC), and vitrinite reflectance (R_o , which reflects the thermal maturity). In addition, T, TOC, R_o , and porosity have effects on V_L . The qualitative relationships between Langmuir and geological parameters are shown in **Table 2**.

Table 2
Qualitative relationships between Langmuir and geological parameters based on literature values [23, 37-43]

	TOC	R_o	T	Porosity
V_L	Positive	Negative	Negative	Positive
P_L	Negative	Negative	Positive	

Microscopically, the abundance of pores directly affects the adsorption capacity. Organic matter offers numerous pores, leading to large surface area and adsorption capacity [69]. This indicates that organic matter is not only hydrocarbon-generation matter, but also the carrier of adsorbed gas. So, P_L decreases and V_L increases with a higher TOC. Regarding thermal maturity, it reflects the thermal evolution degree of shale formations. Thus, within certain limits, a higher R_o represents a higher hydrocarbon-generation potential [13, 66]. However, this does not guarantee low P_L and high V_L values for the following reasons. On the one hand, R_o means vitrinite reflectance, which increases while organic carbon decomposes and becomes more mature [65]. A higher R_o gives less organic carbon, and therefore reduces adsorbed gas potential. On the other hand, the organic carbon maturing process includes dehydrogenation and deoxygenation [70, 71], which will form pores in the microscopic structure and increase adsorbed gas potential [72, 73]. So, the influence of R_o on adsorption ability should be determined by experimental results rather than speculation. In fact, adsorption experimental data indicate that R_o is negatively correlated with both P_L and V_L . Temperature is also an important factor for P_L and V_L . According to Le Chatelier's principle, the increase of temperature inhibits the adsorption process, an exothermic process, which leads to lower adsorption capacity. Finally, the increase in temperature results in the increase of P_L and decrease of V_L .

Regarding the variable selection of the P_L submodel, T, R_o , and TOC are chosen as the independent variables. For the sake of simplicity, the number of independent variables should be reduced by creating interaction terms and making the model three-dimensional. From the analysis above, we know that R_o has a negative correlation with P_L , while there is a positive correlation between P_L and T. Thus, according to the qualitative relationships between these independent variables, the interaction terms $\frac{T}{R_o}$ could be considered as a new independent variable to fit the P_L submodel.

Regarding the variable selection of the V_L submodel, R_o and porosity are eliminated based on data size, correlation coefficient between variables, and the cross-validation results. The data size is counted for each pair of variables. For instance, the data size of T vs. TOC means the number of data points which have effective V_L , T, and TOC simultaneously. The “effective data” here holds the same definition as that in Section 2. Correlation tests between different independent variables are then validated. The original dataset is given in the online supplementary Table C. The results are shown in **Table 3**.

Table 3

Data sizes and correlation coefficients between different independent variables

	Data Size	Correlation Coefficient (absolute value)
T vs. TOC	200	0.26
T vs. R_o	95	0.64
T vs. Porosity	67	0.32
TOC vs. R_o	80	0.45
TOC vs. Porosity	88	0.57
R_o vs. Porosity	34	0.39

As shown in **Table 3**, there is a relationship between R_o and the other variables. The absolute correlation coefficient between T and R_o is as high as 0.64, and that of TOC and R_o is 0.45, which means that they are both moderately correlated [74]. In principle, R_o increases while organic carbon decomposes, indicating a negative correlation between R_o and TOC. In addition, reservoir temperature affects the organic carbon maturing process, which is also measured by R_o . This means that the effect of TOC and T in this model may replace the one of R_o . Moreover, the data sizes of TOC vs. R_o is only 80. The V_L dataset only consists of 79 data points if the model takes all of the TOC, T, and R_o as variables. However, the data size has a 2.5-fold increase to 200 by cutting out R_o . In conclusion, on the one hand, R_o is statistically and theoretically related to T and TOC. On the other hand, the availability of R_o restricts the data size. So, it is reasonable to use T and TOC to substitute the effect of R_o for the simplification of the model. According to the cross-validation results (Section 4.1 presents the process in detail), the elimination of R_o actually increased the model accuracy. The average relative error decreased slightly from 25.75% of the model with R_o to 23.76% without R_o . Furthermore, the half-width of the 90% confidence interval of relative errors dropped from 5.04% with R_o to 2.33% without R_o , which indicates that the estimation accuracy of the model with R_o has a higher fluctuation. The elimination of R_o not only reduces the model dimensionality, but also expands the data size, which results in a more accurate estimation model.

Similarly, porosity is eliminated in the process. On the one hand, the size of the V_L dataset can be expanded from 66 to 200 by leaving it out. On the other hand, the TOC and porosity are moderately correlated with the correlation coefficient of 0.57. This positive correlation has been observed in former studies [75]. Wang et al. determined that the porosity of organic matter in shale is higher than that of mineral matrix [76], which theoretically explicates the moderate correlation. Only one variable between TOC and porosity needs to be considered in the model. Since there are 200 data points that have T and TOC, and the correlation coefficient is only 0.26, porosity was substituted by TOC and T in the model. Furthermore, the cross-validation results show that the average relative error of the model with porosity (27.98%) is higher than the model without porosity (23.76%). In addition, the half-width of the 90% confidence interval of the model with porosity is 5.78%, which is more than two times larger than that of the model without porosity (2.33%). Thus, the V_L submodel takes T and TOC as the independent variables.

3.2 Outlier detection

Outlier detection is essential because of the discrepancy of data sources and the uncertainty

of geological parameters. Since geological variables have continuity, and the relationships between Langmuir parameters and geological variables are monotonous, the K-Nearest Neighbors algorithm (K-NN) is suitable for outlier detection [25-27, 35, 36]. The main idea of the K-NN algorithm is to classify the test data according to the k nearest training samples [77]. If the test data's property value does not match that of the training samples, the test data are considered to be an outlier and should be rejected. In this work, we define the weighted relative error (R_i) as the criterion of outlier detection, which means the relative difference between the i^{th} test data's dependent variable value and the average value of the k nearby training samples. In this research, k is assigned to be 5 and the weighted relative error is defined with 1-norm, which is shown in **Eq. (2)**. The detailed formula derivation process is shown in **Appendix A**. The test data are regarded as an outlier if R_i is greater than the given threshold. The denominator of R_i is the smaller one of the test data's dependent value and the average value of training samples, while the numerator is the weighted sum of the difference between each training sample and test data. There is an inverse relationship between the weight and the distance to the neighbor, which means that the statistically nearer neighbors matter more than the statistically distant ones. The sum of the weights is equal to 1 for every test data.

$$R_i = \frac{\sum_{j=1}^k wR_{i,j} \times |V_{L,i} - V_{L,i,j}|}{\min\left(\frac{\sum_{j=1}^k V_{L,i,j}}{k}, V_{L,i}\right)} \quad (2)$$

where $V_{L,i}$ is the dependent variable value of the i^{th} test data; $V_{L,i,j}$ represents the dependent variable value of the j^{th} neighboring training data of the i^{th} test data; $wR_{i,j}$ is the weight of the dependent value difference between the i^{th} test data and the j^{th} neighboring training data; and $wR_{i,j}$ is very significant, and this weight is calculated based on the "distance" between the test data and training data. Although the detailed calculation process is given in **Appendix A**, it is essential to introduce the "distance", since it is fundamental to determine the k nearest training samples and calculate the weight. First of all, this "distance" should not be the spatial distance, because the spatial relative location cannot precisely describe the similarity in adsorption ability between two different samples in the shale formation. The statistical distance which is based on geological parameters is applied to measuring the "distance" between different samples, in the form of Euclidean distance. Secondly, only the relative values of the variables in their distribution matter, and the absolute values are insignificant in the calculation of the statistical distance. Thus, the Euclidean distance should be adjusted, and it is necessary to perform normalization on these variables. As a result, the weighted Euclidean distance, which is a statistical distance, is computed to determine the k nearest neighbors and assign different weights to different samples.

There are 301 data points in the original dataset before the outlier detection, consisting of 101

P_L data points and 200 V_L data points. According to **Eq. (2)**, the weighted relative error (R) of each data point is calculated based on the K-NN algorithm. The results are shown in the online supplementary material Table B. If the R value of a data point is larger than 0.85, this data point is regarded as an outlier. Regarding the P_L submodel, the weighted Euclidean distance is computed by the TOC, T, and R_o . After outlier detection, 10 data points are deleted, comprising 9.9% of the original data. Finally, 91 data points remain to fit the P_L submodel. As for V_L , the weighted Euclidean distance is calculated based on T and TOC. According to R values, there are 16 data points deleted, taking up 8% of the original data. Finally, 184 data points remain to develop the V_L submodel.

3.3. Model regression

The regression submodels were developed based on the processed data. The model construction process includes the following steps. First, according to previous qualitative studies [23, 37-43], the selected variables are combined to construct functions, which have clear physical meaning and succinct form. Second, mathematical adjustments are applied to variables to better describe the trend of these variables. Then, the P_L and V_L submodels are derived from the processed data, and the coefficients are identified by ordinary least square method (OLS) based on a normal equation [78]. Finally, the multivariate regression model between Langmuir and geological parameters is built based on the P_L and V_L submodels. This regression model can be used for adsorbed gas estimation.

Based on the cleaned data and qualitative relations, the simplified P_L and V_L submodels were constructed. A decay characteristic of Langmuir parameters could be observed in the data scatter plot. Thus, logarithmic treatment is applied to the dependent variables. The adjusted P_L and V_L submodels are shown in **Eq. (3)** and **(4)**, respectively. TOC^* represents dimensionless total organic carbon and is equal to $\frac{TOC}{4\%}$. T^* stands for $\frac{T}{48^\circ C}$. It is the dimensionless adsorption temperature.

R_o^* means the dimensionless thermal maturity, which is equal to $\frac{R_o}{1.75\%}$. In this model, 4%, 48°C, and 1.75% are the average value of TOC, T, and R_o , respectively.

$$\ln P_L = a_p \cdot TOC^* + b_p \cdot \ln\left(\frac{T^*}{R_o^*}\right) + c_p \quad (3)$$

$$\ln V_L = a_v \cdot TOC^* + b_v \cdot T^{*3} + c_v \quad (4)$$

Using 91 data points as fitting data, the coefficients in the P_L submodel were determined, which are $a_p = -0.136$, $b_p = 0.715$, and $c_p = 1.666$. All of the variables are monotonously related to P_L in the model. There is a positive correlation between P_L and T, a negative correlation between P_L and TOC, and a negative correlation between P_L and R_o . These correlations match the qualitative analyses from previous work [23, 37-43]. **Fig. 3a** shows the distribution of P_L data points and its comparison with the regression model. The blue points represent the data for regression, and the red stars are outliers detected by R value and the K-NN algorithm. Regarding

the V_L submodel, the coefficients were obtained from fitting the regression model, which are: $a_v = 0.421$, $b_v = -0.067$, and $c_v = 0.563$. **Fig. 3b** shows the distribution of V_L data points and the outliers. It compares all of the V_L data points with the regression model. The regression model fits the experimental data well by visual comparison. As **Fig. 3b** shows, V_L increases with decreasing T and increasing TOC. These results match the qualitative relationships mentioned in previous work [23, 37-43].

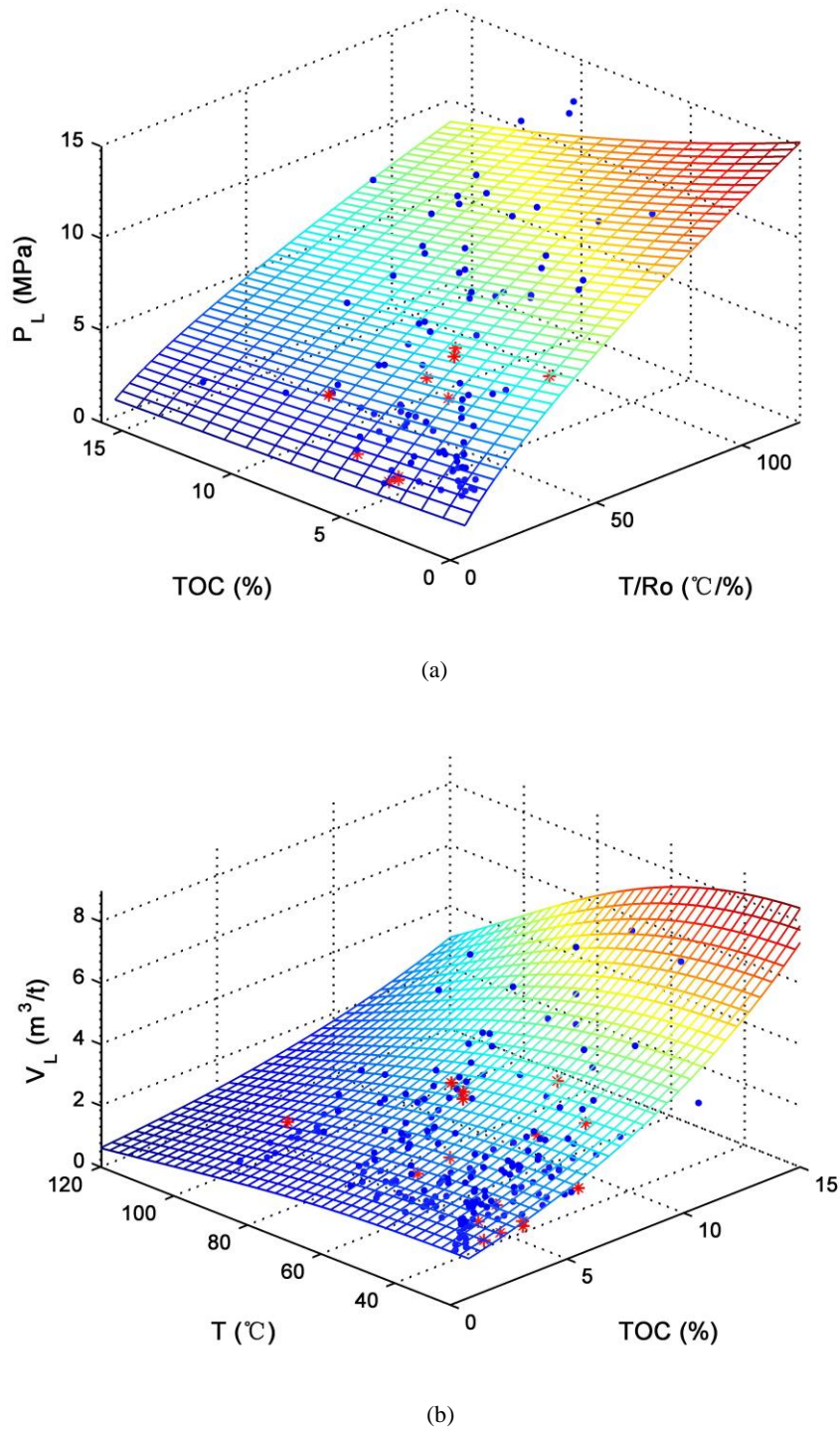


Fig. 3. Comparison of fitting data and outliers with the regression model: (a) P_L data set and P_L model; and (b) V_L

data set and V_L model. The blue points describe the distribution of P_L and V_L data. The red stars represent the outliers in the model. The color grids show the regression model.

4. Model Assessment

4.1. Model validation

The visual comparison in **Fig. 3** is intuitive, but not precise. In order to obtain a reliable and stable model, cross-validation is necessary for the P_L and V_L submodels. The leave-one-out method [28-32] is used for cross-validation in this research. This method involves using one observation as the validation sample and taking the remaining data as the training set. The training set is utilized to fit the validation model, and the relative error is calculated by the validation sample.

When implementing the cross-validation, a vectorizing treatment can simplify the calculation. To vectorize the problem, three matrices are defined. Matrix X includes the original data points, of which each line describes an experimental data point, and each column corresponds to an independent variable. Matrix W is the coefficient matrix of the regression model. Matrix Y includes the values of the dependent variable of experimental data points. The P_L submodel is taken as an example to introduce the vectorizing process. The x_{in} (for $i=1, 2, 3\dots m$) is assumed to be 1. Thus, the w_n represents the constant term in the model. The relationship of these matrices is shown in **Eq. (5)**.

$$\begin{bmatrix} x_{1,1} & \cdots & x_{1,n} \\ \vdots & \ddots & \vdots \\ x_{m,1} & \cdots & x_{m,n} \end{bmatrix} \times \begin{bmatrix} w_1 \\ \vdots \\ w_n \end{bmatrix} = \begin{bmatrix} P_{L,1} \\ \vdots \\ P_{L,m} \end{bmatrix} \quad (5)$$

The relative error between the validation sample and the training set is the indicator of the model quality. In the cross-validation process, all of the data points should be treated as a validation sample once. The i^{th} data point is taken as an example to illustrate the leave-one-out process. The function to calculate the i^{th} relative error is defined in **Eq. (6)**. $P_{L,i}$ is the experimental dependent variable of the i^{th} data point, and $P'_{L,i}$ is the estimation of the dependent variable of the i^{th} data point. This relative error is different with the weighted relative error (R) in **Eq. (2)**. The weighted relative error (R) is based on K-NN algorithm and is only used in the outlier detection process. **Eq. (7)** presents the method to calculate $P'_{L,i}$, where X_i is constructed with all of the data except the i^{th} data point. The detailed formula derivation process is shown in **Appendix B**. The above process is repeated m times until all of the m samples are considered as validation data once. Finally, the relative errors of all samples are averaged to represent the accuracy of the P_L and V_L submodels. The confidential interval is calculated, as well.

$$Error_i = \frac{P_{L,i} - P'_{L,i}}{P_{L,i}} \times 100\% \quad (6)$$

$$P'_{L,i} = [x_{i,1} \quad \cdots \quad x_{i,n}] \times (\mathbf{X}_i^T \mathbf{X}_i)^{-1} \mathbf{X}_i^T \begin{bmatrix} P_{L,1} \\ \vdots \\ P_{L,i-1} \\ P_{L,i+1} \\ \vdots \\ P_{L,m} \end{bmatrix} \quad \text{where } \mathbf{X}_i = \begin{bmatrix} x_{1,1} & \cdots & x_{1,n} \\ \vdots & \ddots & \vdots \\ x_{i-1,1} & \cdots & x_{i-1,n} \\ x_{i+1,1} & \cdots & x_{i+1,n} \\ \vdots & \ddots & \vdots \\ x_{m,1} & \cdots & x_{m,n} \end{bmatrix} \quad (7)$$

Regarding the P_L submodel, all of the 91 data points are separately used as the validation data in the leave-one-out process. Finally, the average relative error with the 90% confidential interval is $27.67 \pm 3.54\%$. Considering the great variety of data sources, shale locations and shale types, this error is acceptable. The cross-validation result attests to the accuracy of the model. Furthermore, although the training data are different in every validation test, all of the fitting models are similar to the final regression model, which means that this model is robust and not sensitive to the training data. Based on the cross-validation results, **Fig. 4** shows the distribution of the experimental values, the estimated values, and the relative error between the experimental and estimated data. **Fig. 4a** presents the scatter of the experimental values versus their corresponding estimated values. The closer the distribution of points is to the 45° diagonal, the better the estimation. **Fig. 4b** is a normal Q-Q plot of the 91 average relative errors. This figure compares the probability distribution of the average relative errors with the normal distribution by plotting their quantiles against each other. The reference line represents the ideal condition when the relative errors obey the normal distribution exactly. It is clear from **Fig. 4** that the estimated values are similar to the experimental ones, and the relative errors are approximately normally distributed. Regarding the V_L submodel, all of the 184 data points are used as the validation data. The relative errors are calculated just like for the P_L submodel. Finally, the average relative error is 23.76%, with its 90% confidence interval being (21.43%, 26.09%). The confidence intervals are calculated based on a fixed-sample-size procedure [79]. **Fig. 5a** shows the scatter of the experimental values versus the estimated values, and **Fig. 5b** presents the Q-Q plot of the relative errors versus the normal distribution. As shown in **Fig. 4b** and **Fig. 5b**, there is a deviation between the expected normal values and average relative errors when the expected normal value increases beyond 40%. This deviation is resulted from the following two reasons. Firstly, the acceptance region of Q-Q plot is not parallel to the reference line. The acceptance region becomes wider when the quantile gets closer to 0 or 1 (corresponding to the bottom left and upper right of the Q-Q plot) [80, 81]. Secondly, the model has less data points with large positive error compared with the normal distribution, which results in the phenomena that expected values are above the reference line on the upper right. This actually means that the relative error in the model is apt to be smaller than that in the normal distribution when the error is above 40%. In addition, the 40% relative error corresponds to the 91% quantile in standard normal distribution. Thus, the deviation in the Q-Q plot actually only affects a small proportion of the data, and this means that there are fewer positive errors in the model than the normal distribution.

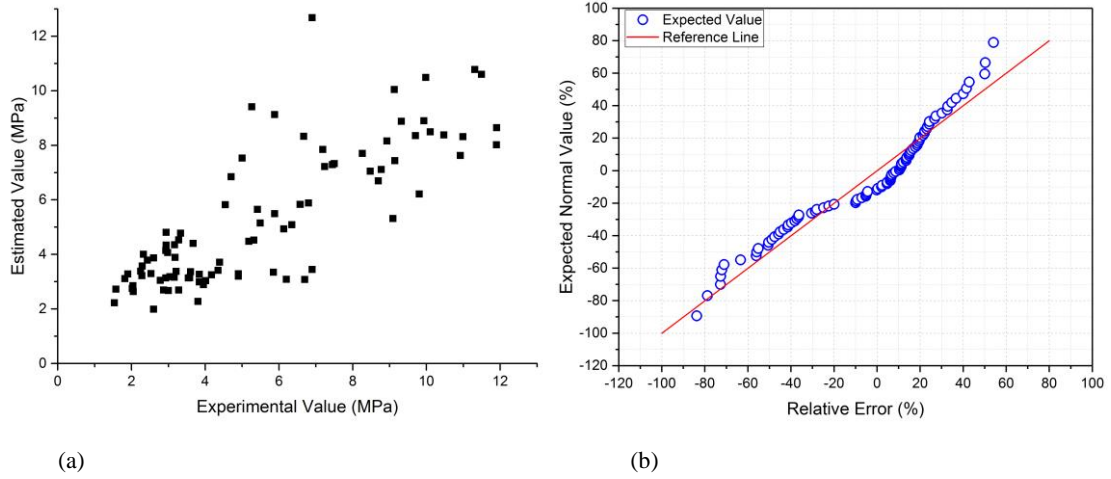


Fig. 4. Results of the P_L submodel's cross-validation: (a) the scatter of the experimental value versus its corresponding estimated value; and (b) the Q-Q plot of the distribution of the relative errors versus the normal distribution.

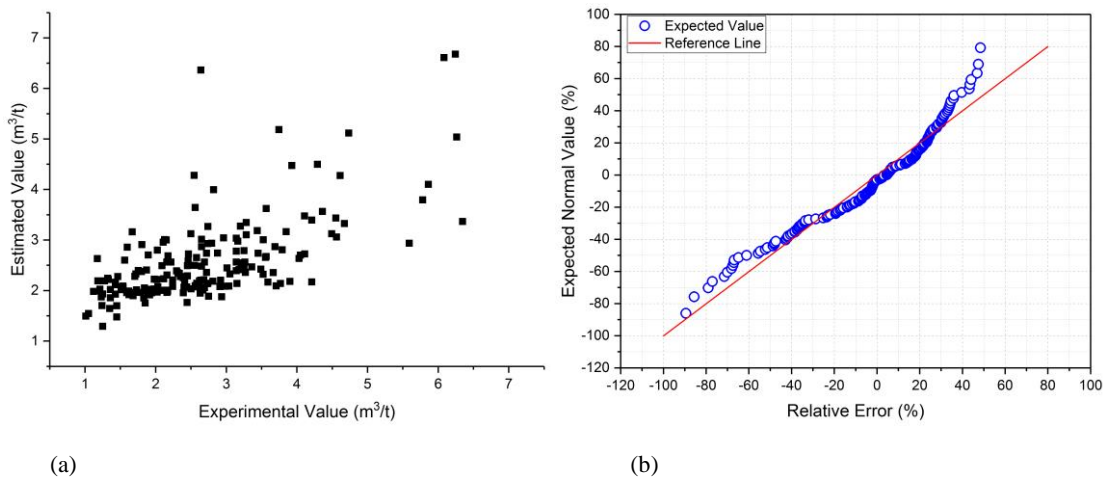


Fig. 5. Results of the V_L submodel's cross-validation: (a) the scatter of the experimental value versus its corresponding estimated value; and (b) the Q-Q plot of the distribution of the relative errors versus the normal distribution.

4.2. Model comparison

Some previous work has already proposed a couple of P_L and V_L submodels based on geological parameters, as listed in **Table 4** [23, 44-46, 82]. However, the inadequate training data and the lack of independent variables affect the estimation accuracy and applicability of these models. Most of those studies' training sets have less than 10 data points due to the time-consuming adsorption experiments and the expensive coring process. Previous models and the model developed in this research were compared by calculating the average relative errors. The process is as follows. First, the training data are randomly extracted from the entire dataset to fit the regression model. The proportion of the training data is 80% and 90% for the P_L and V_L submodels, respectively. Then, the other 20% (for the P_L submodel) and 10% (for the V_L

submodel) of the entire data are used as the test data for the average relative error calculation to validate the model. Since the economically attractive shale gas reservoirs always have relatively high TOC and high R_o , it is also essential to compare the different models under these conditions. The extraction and validation process are performed 14 times for the P_L submodels and 11 times for the V_L submodels. The first five times for each model are of the entire dataset extraction, which means that the test data are extracted randomly from all of the 91 data points for the P_L submodels and from the 184 data points for the V_L submodels. The next three times are for the high temperature scenario, in which the test data are stochastically sampled from the data whose temperature is higher than 65°C . There are also three comparisons belonging to the high TOC scenario, in which the test data are taken from the data whose TOC are higher than 5%. The last three comparisons of the P_L submodels are for the high R_o scenario, in which the test data are extracted from the data with R_o higher than 2%. Finally, the fitting precisions of these models are compared based on the cross-validation results.

Table 4
Different P_L and V_L submodels from previous studies

Literature	Model
[46]	$\ln \frac{1}{P_L} = \frac{a}{T} + c$
[82]	$P_L = a \times TOC^{-b}$
[82]	$V_L = a \times TOC^b$
[23, 44-46]	$V_L = a \times TOC + b$

Concerning the P_L submodels, 18 data points are extracted from the P_L dataset as the test data. The validation process is repeated 14 times. The calculation results are shown in **Table 5**. The overall average relative error of the proposed P_L submodel is 25.13%, which is much less than the 35.90% and 40.04% from the existing models. In the high temperature scenario, the comparisons between the existing and new models are independently conducted three times. Since the shale gas reservoirs are generally deep, many reservoirs' temperatures are higher than 65°C [83-87]. The average relative errors of the existing models are 47.77% and 42.56%, and that of the new model is 26.25% in the high temperature scenario, indicating that the new model possesses an advantage over the previous ones. Considering real-world applications, the high TOC and high R_o scenarios should be examined as well, because commercially attractive shale gas reservoirs always have high TOC and R_o . The advantage of the new model is obvious in these scenarios. The average relative errors decrease from 46.01% and 48.20% (the existing models) to 27.52% (the new model) under the high TOC condition. In the high R_o scenario, the errors drop from 60.52% and 71.33% (the existing models) to 33.60% (the new model). It is clear that the new model's average relative errors are much less than the existing models from the literature, not only under the overall condition but also in the circumstances of high temperature, high TOC, and high R_o . Considering real-world situations, the new P_L submodel is more useful and accurate.

Table 5
Relative error comparison of the P_L submodels in different scenarios

Test Number	Relative Error (%)		
	$\ln \frac{1}{P_L} = \frac{a}{T} + c$	$P_L = a \times TOC^{-b}$	$\ln P_L = a \times TOC^* + b \times \ln \frac{T^*}{Ro^*} + c$
Test 1	40.78	35.21	23.42
Test 2	35.20	45.14	27.56
Test 3	23.74	32.61	22.15
Test 4	48.88	52.02	30.51
Test 5	30.89	35.19	21.99
Average	35.90	40.04	25.13
HighT1	50.15	44.54	24.84
HighT2	52.54	43.11	28.01
HighT3	40.63	40.02	25.89
Average	47.77	42.56	26.25
HighTOC1	30.51	33.26	26.20
HighTOC2	46.78	40.52	26.57
HighTOC3	60.74	70.82	29.79
Average	46.01	48.20	27.52
HighRo1	55.39	79.44	32.44
HighRo2	67.91	70.30	39.78
HighRo3	58.26	64.26	28.57
Average	60.52	71.33	33.60

For the V_L submodel, the new model is compared with the existing models in different scenarios, as well. **Table 6** shows the validation results. According to **Table 6**, the average relative error of the new model is 23.87%, which is less than 25.42% and 25.79% for the existing models, among the five entire dataset extraction tests. This means that the new model is more accurate, in general. Furthermore, regarding the high temperature scenarios, the average relative errors are 38.45% and 39.59% for the existing models, and 23.34% for the new model. This means that the introduction of the temperature term to the model reduces the relative error by more than 15%. Furthermore, the three tests with high TOC indicate that the new V_L submodel has a similar performance to the existing models. As such, the new P_L and V_L submodels are statistically better than the existing models, especially under real-world conditions. Therefore, the proposed P_L and V_L submodels could be applied to Langmuir parameters estimation under real-world conditions.

Table 6

Relative error comparison of the V_L submodels in different scenarios

Test Number	Relative Error (%)		
	$V_L = a \times TOC^b$	$V_L = a \times TOC + b$	$\ln V_L = a \times TOC^* + b \times T^{*3} + c$
Test 1	23.34	21.24	21.27
Test 2	29.32	30.86	23.06

Test 3	26.07	27.52	25.06
Test 4	24.68	26.36	25.67
Test 5	23.68	22.98	24.30
Average	25.42	25.79	23.87
HighT1	35.16	38.11	20.49
HighT2	45.82	45.56	27.27
HighT3	34.39	35.10	22.27
Average	38.45	39.59	23.34
HighTOC1	23.42	24.87	22.44
HighTOC2	25.43	25.17	25.46
HighTOC3	23.08	28.12	24.42
Average	23.98	26.05	24.11

5. Geological-parameter-based estimation model

Since the Langmuir model is the most commonly used empirical model to estimate adsorbed gas content, we propose a new model for estimating the adsorbed gas content on the basis of the P_L and V_L submodels presented in the above. By plugging **Eq. (3)** and **(4)** into the Langmuir model (**Eq. (1)**), the P_L and V_L terms can be substituted by geological parameters, such as reservoir temperature, TOC, and R_o . All of these geological parameters can be determined without adsorption experiments. By replacing the Langmuir parameters with the geological parameters, the classical Langmuir model can be transformed to the new geological-parameter-based estimation model in **Eq. (8)**. This model only depends on the directly measurable geological parameters. The adsorbed gas content can be easily estimated by the reservoir depth h , TOC, R_o , reservoir pressure, and temperature. The regression coefficients, a_p , b_p , c_p , a_v , b_v , and c_v are from the P_L and V_L submodels. They are constants when the training database is fixed.

$$V = \frac{V_L}{1 + \frac{P_L}{P}} = \frac{\exp(a_v \cdot TOC^*) \cdot \exp(b_v \cdot T^{*3}) \cdot \exp(c_v)}{1 + \frac{1}{P} \cdot [\exp(a_p \cdot TOC^*) \cdot (\frac{T^*}{R_o^*})^{b_p} \cdot \exp(c_p)]} \quad (8)$$

Although the reservoir temperature and pressure in **Eq. (8)** can be measured directly, they can also be estimated when it is difficult to determine them. The reservoir temperature can be calculated by the reservoir depth (h), the surface temperature and the temperature gradient ($\text{grad}T$), as shown in **Eq. (9)**. In addition, the reservoir pressure can be determined by the reservoir depth and the pressure coefficient (α) as **Eq. (10)**. \vec{n} is a normal unit vector, which is dimensionless.

The reservoir isothermal surfaces are assumed to be horizontal, and thus the direction of \vec{n} is vertically downward, which is the same as the reservoir depth's direction. T_s represents the surface

temperature, °C. P_h means the hydrostatic pressure, or the pressure exerted by the column of water above the formation, MPa. It can be estimated by the water density and the reservoir depth.

α is the pressure coefficient, which is dimensionless. ρ_w represents water density equal to 1, t/m³.

g is the local acceleration of gravity equal to 9.8, N/kg.

$$T = h \cdot \text{grad}T + T_s = h \cdot \frac{\partial T}{\partial n} \cdot \vec{n} + T_s \quad (9)$$

$$P = \alpha \cdot P_h = \alpha \cdot \rho_w \cdot g \cdot h = 9.8 \cdot \alpha \cdot h \quad (10)$$

6. Case study: Adsorbed gas content estimation of nine shale gas reservoirs

To estimate the adsorbed gas content in different reservoirs, the values of the geological parameters in different reservoirs should be determined accordingly. In this study, the following reservoirs in China, Germany, and the U.S.A. are examined: the Sichuan Basin, the Yangtze Platform, the Songliao Basin, the Ordos Basin, the Tarim Basin, the Northern Jiangsu Basin, the Marcellus Shale, the Barnett Shale, and the Posidonia Shale. The Marcellus Shale and the Barnett Shale are from the U.S.A., and the Posidonia Shale is from Germany. The remaining six reservoirs are in China.

The data of TOC and R_o were collected from previous work, which are shown in **Table 7**. **Fig. 6** presents the distribution of TOC and R_o data for different reservoirs. It is clear from **Fig. 6a** that both the mean and median of TOC of all basins are higher than 2%, which is the commercial development threshold [13, 65]. **Fig. 6b** shows that, except for the Northern Jiangsu Basin, the Songliao Basin, the Barnett Shale, and the Posidonia Shale, the mean and median of other reservoirs' R_o are higher than 1.3%. The R_o values indicate that these reservoirs are relatively mature and have passed the oil window [88]. Regarding the Yangtze Platform, the Sichuan Basin, and the Marcellus Shale, their R_o values exceed 2%, which indicates that they are already in a dry gas window [13, 70, 89, 90]. The R_o distribution implies that the organic matter of these shale gas reservoirs is highly matured, and this explains why these shale reservoirs mainly produce shale gas, but not shale oil. Concerning the reservoir temperature, the Global Heat Flow Database provided by the International Heat Flow Commission [91] contains temperature gradient data from all around the world. The temperature gradient data within China, Germany, and the U.S.A. have 667, 254, and 4249 data points, respectively. The inverse distance weighting (IDW) interpolation method [92-94] is used to calculate reservoir temperature since temperature is a continuous variable underground. This interpolation method assumes that the value of an unsampled point is the weighted average of its neighbor samples. In addition, the weight is inversely related to the distance between the unsampled point and its neighbor. The temperature distribution of each reservoir is calculated in **Appendix C**, and the average temperature is used as the reservoir temperature in the following estimation.

Table 7

TOC and R_o data sizes for different shale reservoirs [48, 95-113]

Reservoir	Sichuan Basin	Yangtze Platform	Songliao Basin	Ordos Basin	Tarim Basin	Northern Jiangsu Basin	Marcellus Shale	Barnett Shale	Posidonia Shale
Amount of TOC data	39	31	6	8	12	10	12	9	18
Amount of R _o data	27	13	5	8	12	10	3	8	18

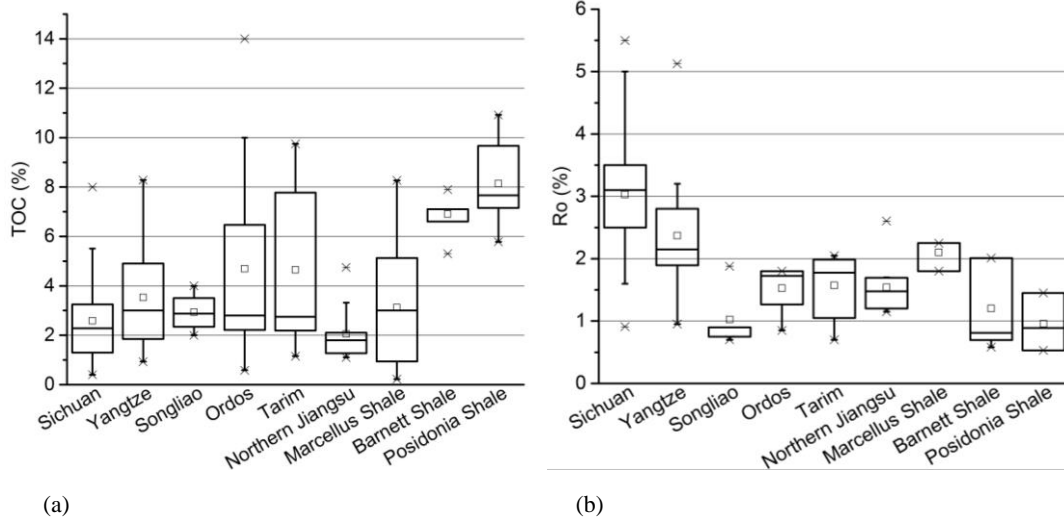


Fig. 6. Distribution of the TOC and R_o data for the Sichuan Basin, the Yangtze Platform, the Songliao Basin, the Ordos Basin, the Tarim Basin, the Northern Jiangsu Basin, the Marcellus Shale, the Barnett Shale, and the Posidonia Shale: (a) the TOC box plot of different reservoirs; and (b) the R_o box plot of different reservoirs. The asterisks represent outliers that are out of the 1.5 IQR (interquartile range). The blank squares correspond to the means of TOC and R_o in different reservoirs.

The geological parameters are evaluated separately, and the results are shown in **Table 8**. To calculate the reservoir pressure, each reservoir pressure coefficient is assumed to be 1. The surface temperature is assumed to be 20 °C when calculating the reservoir temperature in this study. Finally, the adsorbed gas contents are estimated by plugging the geological parameters into the geological-parameter-based estimation model (**Eq. (8)**). The results are shown in the last column of **Table 8** and **Fig. 7**. The observations of adsorbed gas content in the Sichuan Basin, the Ordos Basin, and the Marcellus Shale are shown in **Fig. 7**, as well. Owing to the high cost of adsorption experiments, there is a lack of experimental data about adsorbed gas contents in most reservoirs. However, the Sichuan Basin, the Ordos Basin, and the Marcellus Shale are relatively developed, and some researchers have estimated the adsorbed gas contents. Thus, their data can serve as a reference used to compare the estimation results in this study. According to previous studies, the adsorbed gas content in the Sichuan Basin ranges from 1.12 m³/t to 1.74 m³/t, with the average of 1.28 m³/t [114]. The estimation result in this work is 1.31 m³/t, which is consistent with previous work. Regarding the Ordos Basin, researchers have evaluated the adsorbed gas content in Chang 7 Member and Chang 9 Member of the Yanchang Formation, which are 1.17 - 3.68 m³/t, with the mean of 1.67 m³/t and 1.19 - 2.62 m³/t with the average of 1.32 m³/t, respectively [115]. These results confirmed the estimation in this research, in which the adsorbed gas content is 1.47 m³/t in the Ordos Basin. As for the Marcellus Shale, researchers have shown in a previous study that the adsorbed gas content ranges from 0.85 m³/t to 1.4 m³/t [101]. The estimation of our model is 1.24

m³/t, which confirms with the observation in the previous study. It is thus shown that the experimental results from previous studies validated the estimation in the Sichuan Basin, the Ordos Basin, and the Marcellus Shale from this research. Moreover, the estimation procedure is totally independent of adsorption experiments in this study, which reduces the estimation cost and increases efficiency.

Table 8

Geological parameters and the estimated adsorbed gas contents in China shale gas reservoirs

Reservoir	Depth (m)	TOC (%)	R _o (%)	Reservoir Temperature (°C)	Reservoir Pressure (MPa)	Adsorbed Gas Content (m ³ /t)
Sichuan Basin	3230	2.58	3.03	86.98	31.65	1.34
Yangtze Platform	1737	3.53	2.37	57.48	17.02	1.81
Songliao Basin	1731	2.93	1.03	90.46	16.96	0.92
Ordos Basin	2730	4.69	1.53	86.93	26.75	1.51
Tarim Basin	4023	4.65	1.57	95.99	39.43	1.39
Northern Jiangsu Basin	2872	2.05	1.54	106.19	28.15	0.79
Marcellus Shale	2057	3.12	2.10	87.26	20.16	1.24
Barnett Shale	2286	6.90	1.20	83.23	22.40	1.88
Posidonia Shale	53	8.14	0.96	22.66	0.52	0.52

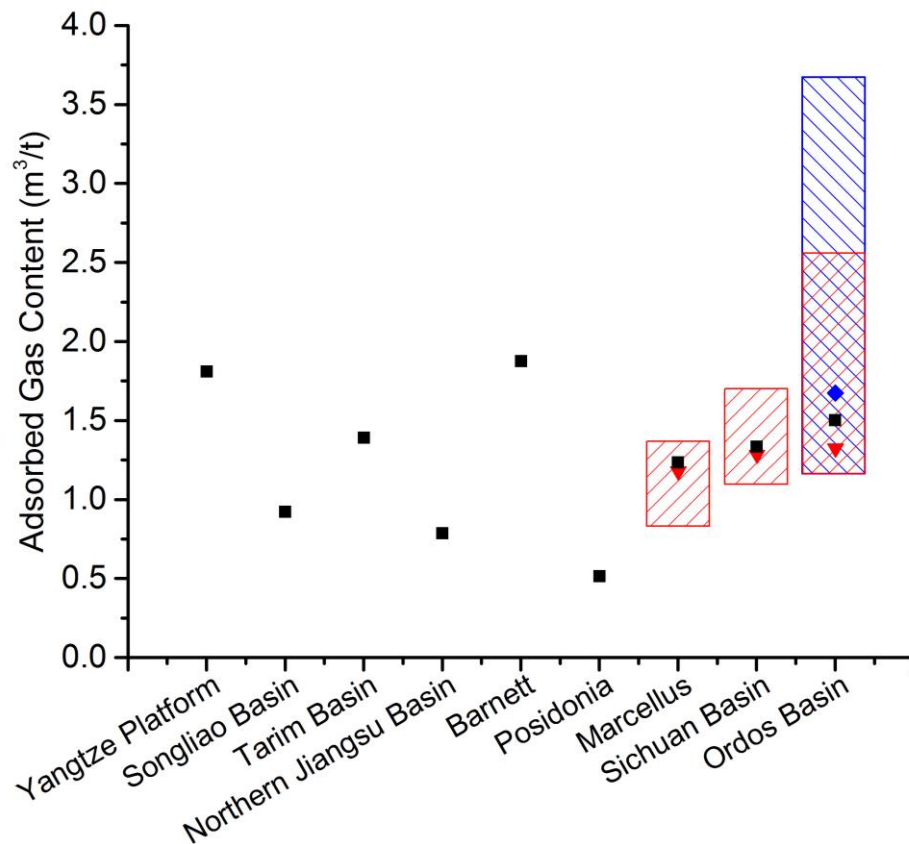


Fig. 7. Comparison of adsorbed gas content estimations and the observations in nine reservoirs. The black squares indicate the estimation values in nine reservoirs. The floating chart shows the distributions of adsorbed gas content

observations in the Marcellus Shale, the Sichuan Basin, and the Ordos Basin. Regarding the Ordos Basin, the red column in the floating chart describes the observations in the Chang 9 Member, and the blue column represents the Chang 7 Member.

7. Discussion and Conclusion

In this study, statistical learning methods were utilized to construct an adsorbed gas content estimation model based on geological parameters. Statistical learning is effective in finding a predictive function, and it can elucidate hidden patterns and unknown correlations between shale gas content and other variables. In the model construction process, 301 data points are collected from different studies, experiment reports, and databases. The outliers are detected by the K-NN algorithm, and the model performance is validated by the leave-one-out cross-validation. Moreover, the usage of geological parameters makes it possible to estimate adsorbed gas content without conducting time-consuming adsorption experiments and an expensive coring process. Thus, the geological-parameter-based estimation model is efficient with a relatively low cost.

Regarding variable selection of the estimation model, more variables may be considered in the model, as long as there are enough data to avoid overfitting. Considering the data availability, we only take T, TOC, R_o , and porosity as candidate variables in this paper. These four variables are also the most commonly used variables in the previous studies. Among the other variables, the clay content is important since the adsorption capacities of clay and kerogen are different. Lu et al. proposed a Bi-Langmuir model that can account for gas adsorption on both clay minerals and kerogen [116, 117]. Although our model can be extended to consider clay content without any change in the regression model, the clay content data are not currently widely available.

It should be mentioned that this model is not a complete substitution for adsorption experiments. However, this model is a good choice for the overall approximate estimation of gas content since it can reduce the estimation cost and increase estimation efficiency. This model also makes it possible to estimate the adsorbed gas content at a large scale, such as a whole reservoir. This model can also be applied to an approximate estimation for a single well at a micro scale when no site-specific measurements have been made. When the exact adsorbed gas content of a sample is expected, adsorption experiments still constitute the optimal choice with the availability of adequate equipment and sufficient time.

The geological-parameter-based estimation model is constructed by substituting the P_L and V_L terms in the classical Langmuir model by two submodels. Compared with the existing P_L and V_L submodels, the new submodels proposed in this research possess an advantage under real-world conditions. Regarding the P_L submodel, the estimation errors decrease to nearly half of that of the existing models in the high temperature scenario, high TOC scenario, and high R_o scenario. The overall average relative error from cross-validation is 27.67 ± 3.54 % with a 90% confidential interval. As for the V_L submodel, the estimation relative error decreases apparently in the high temperature scenario, and is similar to the existing models in the high TOC scenario. The overall average relative error is 23.76%, with its 90% confidence interval being (21.43%, 26.09%). Because most promising reservoirs have high TOC and high R_o , the new submodels perform better under real-world conditions.

Finally, a geological-parameter-based estimation model is developed to estimate adsorbed gas content in shale gas reservoirs, and it is applied to the Sichuan Basin, the Yangtze Platform, the

Songliao Basin, the Ordos Basin, the Tarim Basin, the Northern Jiangsu Basin, the Marcellus Shale, the Barnett Shale, and the Posidonia Shale as case studies. A major advantage of this model is that the whole estimation process is totally independent of time-consuming adsorption experiments and the expensive coring process. As shale gas developments are still in the initial phase in many countries, there are no specific measurements available at most shale gas reservoirs. The model presented in this research provides a reasonably accurate approach to estimate the adsorbed gas contents in different reservoirs around the world with easily-obtained geological parameters.

Acknowledgements

This work is partially funded by the National Natural Science Foundation of China (Grant No. U1262204, 51520105005, and U1663208) and the National Key Technology R&D Program of China (Grant No. 2012BAC24B02). The data used in the estimation model is available in the online supplementary material of this paper.

Appendix. A: Detailed formula derivation process for outlier detection

The outlier detection process is described as follows. First, a distance should be calculated to determine k nearest training samples. As discussed in the body of the text, this “distance” should not be the spatial distance since it is not suitable for measuring the similarity in adsorption ability between two different samples. In addition, it is necessary to perform normalization on the variables due to the different scales of these variables. Thus, a weighted Euclidean distance, which is a statistical distance based on geological parameters, is used to determine the k nearest neighbors and to assign different weights to different samples. The distance is defined in **Eq. (A.1)**.

$$D_{i,j} = \sqrt{\sum_{l=1}^n [w_l^2 \times (x_{l,i} - x_{l,j})^2]} \quad (\text{A.1})$$

where $D_{i,j}$ means the statistical distance between the i^{th} sample and j^{th} sample; $x_{l,i}$ represents the i^{th} sample of the l^{th} variable; and w_l represents the weight of the l^{th} variable. This weight is used for normalization. The most common normalization method is called min-max normalization which performs a linear transformation on the original data [118]. Usually, the new normalized value equals the difference between two points divided by the difference between the maximum and minimum value. This method maps the difference between two points to a value in the range from 0 to 1. However, the normalization process in **Eq. (A.1)** occurs prior to the outlier detection, which means that the data used might be an outlier. If the maximum or minimum values end up to be an outlier, the min-max normalization will be greatly affected, because the denominator in the weight will be abnormally large. To avoid this problem, we replace the difference between maximum and minimum values with the interquartile range (IQR) in this paper. The difference between maximum and minimum values is sensitive to the abnormal values, but the IQR is not.

Finally, w_l is stated as **Eq. (A.2)**. This weight is related to the distribution of variables, and it is essential for the normalization.

$$w_l = \frac{10}{Q_{3,l} - Q_{1,l}} \quad (\text{A.2})$$

where $Q_{1,l}$ and $Q_{3,l}$ represent the upper and lower quartile of the l^{th} variable, respectively.

Using this weighted distance, the impact of different variables on the statistical distance could be evaluated.

The outliers are then detected from the relative difference between the test data and the average value of k nearby training samples. In this research, k is assigned to be 5. The relative difference is defined with 1-norm in **Eq. (2)**, and the weight is shown in **Eq. (A.3)**. The test data are regarded as an outlier if R_i is greater than the given threshold.

$$wR_{i,j} = \frac{\sum_{l=1}^k D_{i,l} - D_{i,j}}{(k-1) \times \sum_{l=1}^k D_{i,l}} \quad (\text{A.3})$$

where $wR_{i,j}$ is the weight of the dependent value difference between the i^{th} test data and the j^{th} neighboring training data; and $\sum_{l=1}^k D_{i,l}$ is the sum of the statistical distances between the i^{th} test data and all of its k neighboring training data.

Regarding the P_L submodel, the weighted statistical distance function is defined as **Eq. (A.4)**. The relative error (R) is calculated according to **Eq. (2)**. The data points whose R values are greater than 0.85 are removed as outliers. Concerning V_L , since the regression model of V_L uses T and TOC as the independent variables, the distance function is defined as **Eq. (A.5)**. The data points whose R value are greater than 0.85 are removed.

$$D_{i,j} = \sqrt{w_T^2 \times (T_i - T_j)^2 + w_{\text{TOC}}^2 \times (\text{TOC}_i - \text{TOC}_j)^2 + w_{\text{Ro}}^2 \times (Ro_i - Ro_j)^2} \quad (\text{A.4})$$

$$D_{i,j} = \sqrt{w_T^2 \times (T_i - T_j)^2 + w_{\text{TOC}}^2 \times (\text{TOC}_i - \text{TOC}_j)^2} \quad (\text{A.5})$$

Appendix. B: Detailed formula derivation process for the leave-one-out method

The i^{th} data point is taken as a validation sample to illustrate the process of leave-one-out cross-validation. First, matrix X and Y are constructed with all data except the i^{th} data point (**Eq. (B.1)**), and then W is calculated according to the normal equation (**Eq. (B.2)** and **(B.3)**) [78].

$$\begin{bmatrix} x_{1,1} & \cdots & x_{1,n} \\ \vdots & \ddots & \vdots \\ x_{i-1,1} & \cdots & x_{i-1,n} \\ x_{i+1,1} & \cdots & x_{i+1,n} \\ \vdots & \ddots & \vdots \\ x_{m,1} & \cdots & x_{m,n} \end{bmatrix} \times \begin{bmatrix} w_1^i \\ \vdots \\ w_n^i \end{bmatrix} = \begin{bmatrix} P_{L,1} \\ \vdots \\ P_{L,i-1} \\ P_{L,i+1} \\ \vdots \\ P_{L,m} \end{bmatrix} \quad (\text{B.1})$$

$$\mathbf{X}_i^T \mathbf{X}_i \begin{bmatrix} w_1^i \\ \vdots \\ w_n^i \end{bmatrix} = \mathbf{X}_i^T \mathbf{Y}_i \quad (\text{B.2})$$

$$\begin{bmatrix} w_1^i \\ \vdots \\ w_n^i \end{bmatrix} = (\mathbf{X}_i^T \mathbf{X}_i)^{-1} \mathbf{X}_i^T \mathbf{Y}_i \quad (\text{B.3})$$

To estimate the dependent variable of the i^{th} data point, the independent variables of the i^{th} data point are multiplied by the matrix \mathbf{W} (Eq. (B.4)). The function to calculate the relative error is defined as Eq. (B.5). The dependent variable of the i^{th} data point is expressed as $P'_{L,i}$. $P_{L,i}$ represents the experimental value of the i^{th} data point's dependent variable.

$$\begin{bmatrix} P'_{L,i} \end{bmatrix} = \begin{bmatrix} x_{i,1} & \cdots & x_{i,n} \end{bmatrix} \times \begin{bmatrix} w_1^i \\ \vdots \\ w_n^i \end{bmatrix} \quad (\text{B.4})$$

$$\text{Error}_i = \frac{P_{L,i} - P'_{L,i}}{P_{L,i}} \times 100\% \quad (\text{B.5})$$

The above steps are repeated m times until all of the samples are considered as validation data once. Finally, the relative errors of all samples are averaged to represent the accuracy of the P_L and V_L submodels.

Appendix. C: Temperature distribution of six Chinese reservoirs

According to the Global Heat Flow Database [91], the scatter of gradT versus the average depth of the measuring section is shown in Fig. C.1. It is obvious that the gradT whose average depth is lower than 500 m fluctuates greatly. This means that the gradT with low depth is easily affected by the variation of the surface temperature. It is reasonable to ignore those data within 500 m, since most of the shale gas reservoirs are much deeper than 500 m in China (99.82% of the risked GIP is deeper than 500 m, and 40.46% is deeper than 3000 m [14]). Finally, there are 348 gradT data remaining to calculate reservoir temperature.

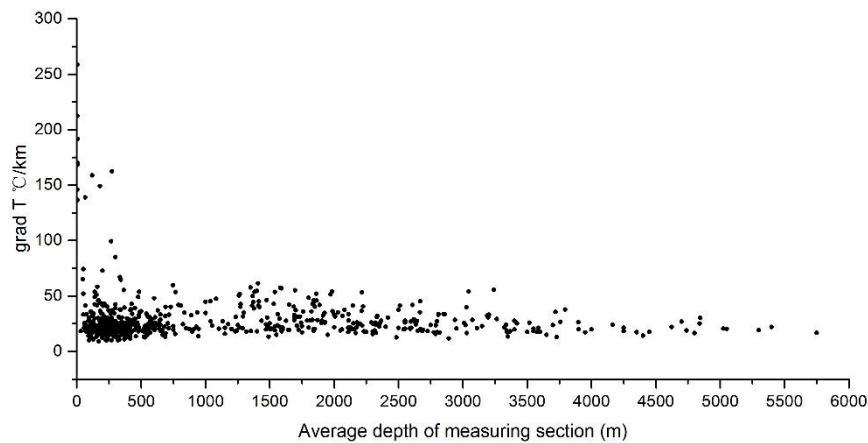


Fig. C.1. Scatter of the gradT versus average depth of the measuring section in China from the Global Heat Flow Database. The gradT whose average depth is lower than 500 m fluctuates greatly.

The reservoir temperature T is the sum of the surface temperature and the additional temperature calculated by gradT and depth. The inverse distance weighting (IDW) interpolation method [92-94] is applied to calculate the additional temperature. Because different shale gas reservoirs have different depths, the nephogram on a certain depth does not accord with the real situation in the reservoirs. Each reservoir's temperature should be calculated only based on this reservoir's average depth and its corresponding gradT. The result is shown in **Fig. C.2**. In this temperature nephogram, the IDW interpolation is applied within each reservoir totally independently from the others.

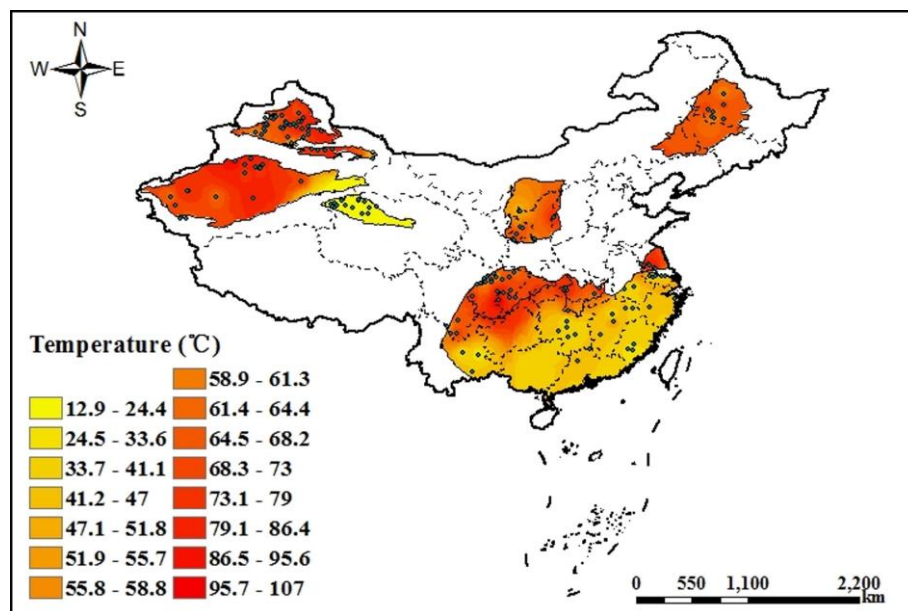


Fig. C.2. Additional temperature nephogram of China based on the real depth of different reservoirs.

References

1. Aguilera, R.F., *The role of natural gas in a low carbon Asia Pacific*. Applied Energy, 2014. **113**:

-
- p. 1795-1800.
2. Stamford, L. and A. Azapagic, *Life cycle environmental impacts of UK shale gas*. Applied Energy, 2014. **134**: p. 506-518.
 3. Arora, V. and Y. Cai, *U.S. natural gas exports and their global impacts*. Applied Energy, 2014. **120**: p. 95-103.
 4. Howarth, R., A. Ingraffea, and T. Engelder, *Natural gas: Should fracking stop?* Nature, 2011. **477**: p. 271-275.
 5. Kerr, R.A., *Natural gas from shale bursts onto the scene*. Science, 2010. **328**(5986): p. 1624-1626.
 6. Yuan, J., D. Luo, and L. Feng, *A review of the technical and economic evaluation techniques for shale gas development*. Applied Energy, 2015. **148**: p. 49-65.
 7. Weijermars, R., *US shale gas production outlook based on well roll-out rate scenarios*. Applied Energy, 2014. **124**: p. 283-297.
 8. Weijermars, R., *Economic appraisal of shale gas plays in Continental Europe*. Applied Energy, 2013. **106**: p. 100-115.
 9. Wang, Z. and A. Krupnick (2013). *A Retrospective Review of Shale Gas Development in the United States: What Led to the Boom?*, Resources for the Future.
 10. Wade, J., et al. (2016). *Natural Gas Annual 2015*, Energy Information Administration (EIA).
 11. Zhang, H. and D. Cao, *Molecular simulation of displacement of shale gas by carbon dioxide at different geological depths*. Chemical Engineering Science, 2016. **156**: p. 121-127.
 12. Yin, H. and Y. Zhang, *A quantitative evaluation method for the effect of temperature on casing collapsing strength: A case study of large-scale hydraulic fracturing in shale gas horizontal wells*. Natural Gas Industry, 2016. **36**(4): p. 73-77.
 13. Kuuskraa, V., S.H. Stevens, and K.D. Moodhe (2013). *Technically recoverable shale oil and shale gas resources: an assessment of 137 shale formations in 41 countries outside the United States*, Department of Energy.
 14. Zhang, D., et al., *China shale gas resource potential evaluation survey*. 2012, Beijing: Geological Publishing House
 15. Wu, Y.-S., et al., *A generalized framework model for the simulation of gas production in unconventional gas reservoirs*. SPE Journal, 2014. **19.05** p. 845-857.
 16. Yin, D., et al., *Shale gas productivity predicting model and analysis of influence factor*. The Open Petroleum Engineering Journal, 2015. **8**: p. 203-207.
 17. Zou, C., *Unconventional Petroleum Geology*. 2012: Newnes.
 18. Ambrose, R.J., et al., *New pore-scale considerations for shale gas in place calculations*, in *SPE Unconventional Gas Conference*. 2010, Society of Petroleum Engineers.
 19. Lewis, R., et al. *New evaluation techniques for gas shale reservoirs*. in *Reservoir symposium*. 2004. Citeseer.
 20. Hartman, R.C., P. Lasswell, and N. Bhatta. *Recent advances in the analytical methods used for shale gas reservoir gas-in-place assessment*. in *San Antonio, Texas, USA: AAPG Annual Convention*. 2008.
 21. Langmuir, I., *The adsorption of gases on plane surfaces of glass, mica and platinum*. Journal of the American Chemical Society, 1918. **40**(9): p. 1361-1403.
 22. Ross, D.J. and R.M. Bustin, *Impact of mass balance calculations on adsorption capacities in microporous shale gas reservoirs*. Fuel, 2007a. **86**(17): p. 2696-2706.

-
23. Wu, J., B. Yu, and Y. Li, *Adsorption capacity of shale gas and controlling factors from the well Yuye 1 at the southeast of Chongqing*. Journal of Southwest Petroleum University(Science & Technology Edition), 2012. **34**(4): p. 40-48.
 24. Vapnik, V.N., *An overview of statistical learning theory*. IEEE Transactions on Neural Networks, 1999. **10**(5): p. 988-999.
 25. Ramaswamy, S., R. Rastogi, and K. Shim, *Efficient algorithms for mining outliers from large data sets*. ACM SIGMOD Record, 2000. **29**(2): p. 427-438.
 26. Zhang, H., et al., *SVM-KNN: Discriminative nearest neighbor classification for visual category recognition*, in *2006 IEEE Computer Society Conference on Computer Vision and Pattern Recognition (CVPR'06)*. 2006, IEEE.
 27. Zhang, M.-L. and Z.-H. Zhou, *ML-KNN: A lazy learning approach to multi-label learning*. Pattern Recognition, 2007. **40**(7): p. 2038-2048.
 28. Evgeniou, T., M. Pontil, and A. Elisseeff, *Leave one out error, stability, and generalization of voting combinations of classifiers*. Machine Learning, 2004. **55**(1): p. 71-97.
 29. Kohavi, R., *A study of cross-validation and bootstrap for accuracy estimation and model selection*, in *International Joint Conference on Artificial Intelligence*. 1995: Montreal, Canada. p. 1137-1145.
 30. Cawley, G.C., *Leave-One-Out Cross-Validation Based Model Selection Criteria for Weighted LS-SVMs*, in *The 2006 IEEE International Joint Conference on Neural Network Proceedings*. 2006, IEEE.
 31. Kearns, M. and D. Ron, *Algorithmic stability and sanity-check bounds for leave-one-out cross-validation*. Neural Computation, 1999. **11**(6): p. 1427-1453.
 32. Larsson, S.H., et al., *Effects of moisture content, torrefaction temperature, and die temperature in pilot scale pelletizing of torrefied Norway spruce*. Applied Energy, 2013. **102**: p. 827-832.
 33. Samuelsson, R., et al., *Moisture content and storage time influence the binding mechanisms in biofuel wood pellets*. Applied Energy, 2012. **99**: p. 105-115.
 34. Marvuglia, A. and A. Messineo, *Monitoring of wind farms' power curves using machine learning techniques*. Applied Energy, 2012. **98**: p. 574-583.
 35. Hu, C., et al., *Data-driven method based on particle swarm optimization and k-nearest neighbor regression for estimating capacity of lithium-ion battery*. Applied Energy, 2014. **129**: p. 49-55.
 36. Kusiak, A., M. Li, and Z. Zhang, *A data-driven approach for steam load prediction in buildings*. Applied Energy, 2010. **87**(3): p. 925-933.
 37. Ross, D.J. and R.M. Bustin, *Shale gas potential of the lower jurassic gordondale member, northeastern British Columbia, Canada*. Bulletin of Canadian Petroleum Geology, 2007b. **55**(1): p. 51-75.
 38. Wu, Q., et al., *Log interpretations and the application of core testing technology in the shale-gas: Taking the exploration and development of the Sichuan Basin as an example*. Acta Petrolei Sinica, 2011. **32**(3): p. 484-488.
 39. Gasparik, M., et al., *Geological controls on the methane storage capacity in organic-rich shales*. International Journal of Coal Geology, 2014. **123**: p. 34-51.
 40. Tan, J., et al., *Shale gas potential of the major marine shale formations in the Upper Yangtze Platform, South China, Part II: Methane sorption capacity*. Fuel, 2014. **129**: p. 204-218.

-
41. Zhao, J., S. Zhang, and L. Cao, *Comparison of experimental adsorption between shale gas and coalbed gas*. *Natural Gas Geoscience*, 2013. **24**(1): p. 176-181.
 42. Kong, D., et al., *The characteristic of adsorption on shales and influence factor*. *Petrochemical Industry Application*, 2013. **32**(9): p. 1-4.
 43. Hao, F., H. Zou, and Y. Lu, *Mechanisms of shale gas storage: Implications for shale gas exploration in China*. *AAPG Bulletin*, 2013. **97**(8): p. 1325-1346.
 44. Weniger, P., et al., *High-pressure methane and carbon dioxide sorption on coal and shale samples from the Paraná Basin, Brazil*. *International Journal of Coal Geology*, 2010. **84**(3-4): p. 190-205.
 45. Chen, S., et al., *Shale gas reservoir characterisation: A typical case in the southern Sichuan Basin of China*. *Energy*, 2011. **36**(11): p. 6609-6616.
 46. Zhang, T., et al., *Effect of organic-matter type and thermal maturity on methane adsorption in shale-gas systems*. *Organic Geochemistry*, 2012. **47**: p. 120-131.
 47. Xia, X., S. Litvinov, and M. Muhler, *Consistent approach to adsorption thermodynamics on heterogeneous surfaces using different empirical energy distribution models*. *Langmuir*, 2006. **22**(19): p. 8063-8070.
 48. Zhai, C. (2013). *Reservoir forming condition and exploration prospect of shale-gas in Qijiang-Renhuan area of southeast Sichuan*. Doctoral Thesis, China University of Geosciences (Beijing).
 49. Ma, D., et al., *Comparison on adsorption and desorption thermodynamics features between shale gas and coalbed methane*. *Coal Science and Technology*, 2015. **43**(2): p. 64-67.
 50. Zhang, J. (2013). *Study of lacustrine shale gas adsorption and desorption in Fuxian, Ordos Basin*. Master's Thesis, Southwest Petroleum University.
 51. Guo, W., et al., *Isothermal adsorption/desorption characteristics of shale gas*. *Journal of Central South University* 2013. **44**(7): p. 2836-2840.
 52. Yang, F., et al., *Comparison analysis on model of methane adsorption isotherms in shales*. *Coal Science and Technology*, 2013. **41**(11): p. 86-89.
 53. Bi, H., et al., *Adsorption characteristic and influence factors of Longmaxi Shale in southeastern Chongqing*. *Natural Gas Geoscience*, 2014. **25**(2): p. 302-310.
 54. Xiong, W., et al., *The reservoir characteristics and isothermal adsorption feature of shale*. *Natural Gas Industry* 2012. **32**(1): p. 113-116.
 55. Feng, Y., Z. Ning, and H. Liu, *Fractal characteristics of shales from a shale gas reservoir in the Sichuan Basin, China*. *Fuel*, 2014. **115**: p. 378-384.
 56. Liu, H. and H. Wang, *Adsorption characteristics and influencing factors of China southern marine shale* *Natural Gas Industry*, 2012. **32**(9): p. 5-9.
 57. Heller, R. and M. Zoback, *Adsorption of methane and carbon dioxide on gas shale and pure mineral samples*. *Journal of Unconventional Oil and Gas Resources*, 2014. **8**: p. 14-24.
 58. Dillmore, R., et al. (2015). *Experimental Characterization of Marcellus Shale Outcrop Samples, and their Interactions with Carbon Dioxide and Methane*, Department of Energy, National Energy Technology Laboratory.
 59. ARI (2014). *Coal and shale property database*.
 60. Rexer, T.F., et al., *High-pressure methane adsorption and characterization of pores in posidonia shales and isolated kerogens*. *Energy & Fuels*, 2014. **28**(5): p. 2886-2901.
 61. Guo, H., et al., *The composition and its impact on the methane sorption of lacustrine shales*

-
- from the Upper Triassic Yanchang Formation, Ordos Basin, China. *Marine and Petroleum Geology*, 2014. **57**: p. 509-520.
62. Beaton, A., et al. (2010). Rock Eval, total organic carbon and adsorption isotherms of the Duvernay and Muskwa formations in Alberta: shale gas data release, Energy Resources Conservation Board, Alberta Geological Survey.
63. Beaton, A.P., et al. (2009a). Rock Eval, total organic carbon, adsorption isotherms and organic petrography of the Colorado Group: shale gas data release, Alberta Energy Resources Conservation Board.
64. Beaton, A.P., et al. (2009b). Rock Eval, total organic carbon, adsorption isotherms and organic petrography of the Banff and Exshaw formations: shale gas data release, Alberta Energy Resources Conservation Board.
65. Alexander, T., et al., *Shale gas revolution*. *Oilfield Review*, 2011. **23**: p. 40-55.
66. Chen, J., et al., *A discussion on the upper limit of maturity for gas generation by marine kerogens and the utmost of gas generative potential: Taking the study on the Tarim Basin as an example*. *Chinese Science Bulletin*, 2007. **52**(1): p. 125-132.
67. Li, Y., H. Nie, and P. Long, *Development characteristics of organic-rich shale and strategic selection of shale gas exploration area in China*. *Natural Gas Industry*, 2009. **29**(12).
68. Nie, H., J. Zhang, and Y. Li, *Accumulation conditions of the Lower Cambrian shale gas in the Sichuan Basin and its periphery*. *Acta Petrolei Sinica* 2011. **32**(6): p. 959-967.
69. Wang, F.P. and R.M. Reed. *Pore networks and fluid flow in gas shales*. in *SPE annual technical conference and exhibition*. 2009. New Orleans, USA: Society of Petroleum Engineers.
70. Wang, Y., *An overview on the maturation indicators of organic matter*. *Sciencepaper Online*, 2009. **2**(9): p. 900-911.
71. Pittion, J. and B. Pradier. *Reflectance of vitrinite as a control of thermal history of sediments*. in *Thermal Modeling in Sedimentary Basins: 1st IFP Exploration Research Conference*. 1985. Carcans, France: Éditions Technip.
72. Ross, D.J. and R.M. Bustin, *The importance of shale composition and pore structure upon gas storage potential of shale gas reservoirs*. *Marine and Petroleum Geology*, 2009. **26**(6): p. 916-927.
73. Jarvie, D.M., et al., *Unconventional shale-gas systems: The Mississippian Barnett Shale of north-central Texas as one model for thermogenic shale-gas assessment*. *AAPG bulletin*, 2007. **91**(4): p. 475-499.
74. Mason, R.D., D.A. Lind, and W.G. Marchal, *Statistics: an introduction*. 1998: Duxbury Pr.
75. Passey, Q.R., et al., *A practical model for organic richness from porosity and resistivity logs*. *AAPG bulletin*, 1990. **74**(12): p. 1777-1794.
76. Wang, F., et al., *Evolution of overmature marine shale porosity and implication to the free gas volume* *Petroleum Exploration and Development*, 2013. **40**(6): p. 819-824.
77. Hodge, V.J. and J. Austin, *A survey of outlier detection methodologies*. *Artificial Intelligence Review*, 2004. **22**(2): p. 85-126.
78. Hastie, T., R. Tibshirani, and J. Friedman, *Linear methods for regression*, in *The elements of statistical learning*. 2009, Springer. p. 43-99.
79. Law, A.M., W.D. Kelton, and W.D. Kelton, *Simulation modeling and analysis*. Vol. 2. 1991: McGraw-Hill New York.
80. Michael, J.R., *The stabilized probability plot*. *Biometrika*, 1983. **70**(1): p. 11-17.

-
81. Barca, E., et al., *GTest: a software tool for graphical assessment of empirical distributions' Gaussianity*. Environmental monitoring and assessment, 2016. **188**(3): p. 1-12.
 82. Zhong, G., et al., *A logging evaluation method for gas content of shale gas reservoirs in the Sichuan Basin*. Natural Gas Industry, 2016. **36**(8): p. 43-51.
 83. Curtis, J.B., *Fractured shale-gas systems*. AAPG bulletin, 2002. **86**(11): p. 1921-1938.
 84. INTEK (2011). Review of emerging resources: US Shale gas and shale oil plays. 135, Energy Information Administration (EIA).
 85. Kargbo, D.M., R.G. Wilhelm, and D.J. Campbell, *Natural gas plays in the Marcellus shale: Challenges and potential opportunities*. Environmental Science & Technology, 2010. **44**(15): p. 5679-5684.
 86. Bowker, K.A., *Development of the barnett shale play, Fort Worth Basin*. AAPG Bulletin, 2007a. **91**(4).
 87. Bowker, K.A., *Barnett shale gas production, Fort Worth Basin: Issues and discussion*. AAPG Bulletin, 2007b. **91**(4): p. 523-533.
 88. Romero-Sarmiento, M.-F., et al., *Quantitative evaluation of TOC, organic porosity and gas retention distribution in a gas shale play using petroleum system modeling: Application to the Mississippian Barnett Shale*. Marine and Petroleum Geology, 2013. **45**: p. 315-330.
 89. Tissot, B.P. and D.H. Welte, *Petroleum formation and occurrence*. 2013: Springer Science & Business Media.
 90. Curtis, M.E., et al. *Investigation of the relationship between organic porosity and thermal maturity in the Marcellus Shale*. in *North American Unconventional Gas Conference and Exhibition*. 2011. The Woodlands, Texas, USA: Society of Petroleum Engineers.
 91. IHFC (2011). Global Heat Flow Database.
 92. Lu, G.Y. and D.W. Wong, *An adaptive inverse-distance weighting spatial interpolation technique*. Computers & Geosciences, 2008. **34**(9): p. 1044-1055.
 93. Zimmerman, D., et al., *An experimental comparison of ordinary and universal Kriging and inverse distance weighting*. Mathematical Geology, 1999. **31**(4): p. 375-390.
 94. Bartier, P.M. and C.P. Keller, *Multivariate interpolation to incorporate thematic surface data using inverse distance weighting (IDW)*. Computers & Geosciences, 1996. **22**(7): p. 795-799.
 95. Pu, B. (2008). Analysis of the reservoir-forming conditions of shale gas potential in Sichuan Basin. Master's Thesis, China University of Petroleum
 96. Zhang, J., et al., *Geological conditions for shale gas reservoir forming in Sichuan basin*. Natural Gas Industry, 2008. **28**(2): p. 151-156.
 97. Cheng, K., et al., *Accumulation conditions of shale gas reservoirs in the Lower Cambrian Qiongzhusi formation, the Upper Yangtze region*. Natural Gas Industry, 2009. **29**(5): p. 40-44.
 98. Zhang, Q., et al., *Geological condition and exploration prospect of shale gas in Kuqa depression*. Journal of Daqing Petroleum Institute, 2010. **34**(6): p. 13-17.
 99. Zou, C., et al., *Geological characteristics, formation mechanism and resource potential of shale gas in China*. Petroleum Exploration and Development, , 2010. **37**(6): p. 641-653.
 100. ARI (2011). World shale gas resources: an initial assessment of 14 regions outside the United States, Energy Information Administration (EIA).
 101. Li, Z. (2011). Preliminary evaluation of shale gas exploration potential in Dongying sag. Master's Thesis, Chengdu University of Technology.
 102. Liu, X., et al., *Geological conditions of shale gas forming in Paleozoic Subei area*. Natural Gas

-
- Geoscience, 2011. **22**(6): p. 1100-1108.
103. Wang, S., et al., *Shale gas exploration potential analysis of Ordos basin*. Natural Gas Industry 2011. **31**(12): p. 40-46.
104. Wang, P., et al., *Accumulation of Lower Cambrian Niutitang shale gas and prediction of potential area in Qiannan Sag*. Natural Gas Geoscience, 2011. **22**(3): p. 518-524.
105. Fang, C. (2012). Evaluation of the reservoir-forming conditions of shale gas potential of the Upper Paleozoic in Eastern Ordos Basin. Master's Thesis, Xi'an Shiyou University.
106. Huang, L., et al., *An analysis of resource potential of Upper Paleozoic shale gas in Guizhong depression*. Geology in China, 2012. **39**(2): p. 497-506.
107. Long, P., et al., *Reservoir-forming conditions and strategic select favorable area of shale gas in the Lower Paleozoic of Chongqing and its adjacent areas*. Earth Science Frontiers 2012. **19**(2): p. 221-233.
108. Mao, J., et al., *Shale gas accumulation conditions of Eastern Region of Liaohe Depression*. Earth Science Frontiers 2012. **19**(5): p. 321-331.
109. Wang, L., et al., *Characteristics of Mesozoic marine black shales and prediction of shale gas prospective area in Qiangtang Basin, Tibet*. Earth Science Frontiers 2012. **19**(3): p. 264-279.
110. Yang, R., W. Cheng, and R. Zhou, *Characteristics of organic-rich shale and exploration area of shale gas in Guizhou province*. Natural Gas Geoscience, 2012. **23**(2): p. 340-347.
111. Cheng, P. and X. Xiao, *Gas content of organic-rich shales with very high maturities*. Journal of China Coal Society, 2013. **38**(05): p. 737-741.
112. Yan, S. (2013). The study on reservoir-forming conditions of shale gas in Xidatan Region of the northern margin of the Qaidam Basin. Master's Thesis, Xi'an University Of Science And Technology.
113. Zhou, Q., et al., *Geological evaluation and exploration prospect of Huayuan shale gas block in Hunan province*. Natural Gas Geoscience, 2014. **25**(1): p. 130-140.
114. Pu, B., et al., *Reservoir-forming conditions and favorable exploration zones of shale gas in Lower Silurian Longmaxi Formation of Sichuan Basin*. ACTA Petrolei Sinica, 2010. **31**(2): p. 225-230.
115. Wang, X., *Lacustrine Shale Gas*. 2014, Beijing: Petroleum Industry Press 224.
116. Wang, H., O. Ajao, and M.J. Economides, *Conceptual study of thermal stimulation in shale gas formations*. Journal of Natural Gas Science and Engineering, 2014. **21**: p. 874-885.
117. Lu, X.-C., F.-C. Li, and A.T. Watson, *Adsorption studies of natural gas storage in Devonian shales*. SPE Formation evaluation, 1995. **10**(02): p. 109-113.
118. Jain, Y.K. and S.K. Bhandare, *Min max normalization based data perturbation method for privacy protection*. International Journal of Computer & Communication Technology, 2011. **2**(8): p. 45-50.